Nanoscale Advances

ROYAL SOCIETY OF CHEMISTRY

PAPER

View Article Online
View Journal | View Issue

Cite this: *Nanoscale Adv.*, 2021, **3**, 5301

Vanadium doped $CaTiO_3$ cuboids: role of vanadium in improving the photocatalytic activity†

Harsha Bantawal,[a] U. Sandhya Shenoy *[b] and D. Krishna Bhat *[a]

Received 22nd June 2021
Accepted 27th July 2021

DOI: 10.1039/d1na00468a

rsc.li/nanoscale-advances

$CaTiO_3$ has attracted enormous interest in the fields of photocatalytic dye degradation and water splitting owing to its low cost, excellent physicochemical stability and structural tunability. Herein, we have developed a simple one pot solvothermal approach which directs V into the Ti sites in the isovalent state during the synthesis of V doped $CaTiO_3$ cuboids. The prediction of reduction in the band gap due to the formation of additional levels just beneath the conduction band edge by the first principles density functional electronic structure study is confirmed by the experimental results. The suppression of charge carrier recombination in 1.0 V leads to the highest photocatalytic activity in the degradation of methylene blue. The percentage degradation of 94.2 indicates its suitability as an excellent catalyst for photocatalytic water treatment.

1. Introduction

Environmental pollution and the energy crisis have become serious problems in the developed and developing countries in the world due to the expeditious growth of population and industrialization.[1,2] Semiconductor materials, mainly oxides and chalcogenides have been found to be the most promising materials which can be used to solve the issue by using them in thermoelectric or photocatalytic applications.[3–8] While thermoelectric materials help scavenge the waste heat and convert them to electricity without the release of harmful gases, the photocatalysis strategy tackles these issues by using sunlight as a green, low cost and renewable resource for generation of hydrogen and degradation of pollutants.[9–12] Metal oxides and their composites have been utilized in energy and environmental remediation due to their ease of synthesis, excellent stability, photo-corrosion resistance and superior efficiency.[4,13–15] Among the metal oxides, $CaTiO_3$, is the first known perovskite material which has sparked research interest due to the above mentioned promising features for the decomposition of water and degradation of harmful organic pollutants.[16–18] An efficient photocatalyst should have a suitable band gap which can effectively harvest the visible region of the solar spectrum, suppressed recombination rate of photoinduced charge carriers and excellent resistance towards photocorrosion.[19–21] The band gap energy of $CaTiO_3$ is about 3.2 eV, as a result, its photocatalytic activity is restricted to the UV portion of the solar spectrum only and hence various strategies like doping, construction of heterostructures and coupling with π-conjugated structures have been utilized in order to reduce the band gap.[18,22–24] Among various strategies, doping foreign atoms in to the lattice of wide band gap photocatalysts has been found to be the promising method as there are three possible sites for doping (Ca, Ti and O). However, dopants are known to introduce bulk defects which can also act as recombination centres of photoinduced charges thus diminishing the photocatalytic efficiency of the material.[25,26] Hence it is imperative to find dopants which can efficiently harvest the solar energy and also can suppress the recombination of photo induced charge carriers. Various dopants such as Ag, Cr, Cu, Er, Eu, Fe, La, N, Na, and Zr have been utilized to improve the photocatalytic efficiency of $CaTiO_3$.[24,27–34] In addition to this, co-doping has been utilized in order to passivate the unoccupied impurity states induced by mono-doped systems and thus suppress the recombination rate of photoinduced charges.[24,27,28]

Recently we reported vanadium to be a promising dopant in $SrTiO_3$ and $BaTiO_3$ for photocatalytic degradation of MB and thermoelectric applications, and found that the site occupancy of the dopant decides the efficiency of the material.[35–37] We know that vanadium is a transition element which can exhibit multiple oxidation states. Hence, substitutional doping requires it to be introduced with isovalent charge in order to avoid the formation of the so-called in-gap states acting as recombination centres due to the formation of oxygen vacancies.[38,39] Hence, there is a dire need to develop a novel and eco-friendly synthetic technique which can avoid the formation of defect states. Herein, for the first time we have synthesized V doped $CaTiO_3$ by a facile one pot solvothermal approach by avoiding high temperature calcination. The experimental results indicated the successful incorporation of V^{4+} into the

[a]Department of Chemistry, National Institute of Technology Karnataka, Surathkal, Mangalore-575025, India. E-mail: denthajekb@gmail.com

[b]Department of Chemistry, College of Engineering and Technology, Srinivas University, Mukka, Mangalore-574146, India. E-mail: sandhyashenoy347@gmail.com

† Electronic supplementary information (ESI) available. See DOI: 10.1039/d1na00468a

lattice of $CaTiO_3$ with a significant reduction in the band gap as predicted by density functional theory (DFT) thereby efficiently harvesting the visible light region of the solar spectrum. The photocatalytic activity of the material was tested using methylene blue (MB) dye as a model pollutant and the doped material was found to be highly efficient as compared to parent $CaTiO_3$.

2. Methods

2.1 Preparation of V-doped $CaTiO_3$

All the chemicals were purchased from Sigma-Aldrich and were used as received. Titanium(IV) isopropoxide (1.47 mL) was dissolved in 10 mL of 2-propanol. To this a calculated amount of vanadyl acetylacetonate was added and stirred for one hour. An appropriate amount of calcium nitrate tetrahydrate and 15 mL of 2 M KOH were added. The resultant mixture was sealed in an autoclave and kept in a hot air oven maintained at 180 °C for 24 hours. The resultant precipitates were washed thoroughly with acetic acid and water. The washed products were dried in an oven at 70 °C for 8 hours. The products obtained by using 0.25, 0.5, 1.0, 1.5 and 2.0 mol% of the V precursor were labelled as 0.25 V, 0.5 V, 1.0 V, 1.5 V and 2.0 V respectively. The samples were characterized using various techniques as given in the ESI†.

2.2 Determination of photocatalytic activity

The photocatalytic efficiency was determined by taking MB dye as a model pollutant. The photocatalytic reactor was fitted with a high-pressure 250 W Hg vapour lamp which was used as a visible light source by using a filter. Prior to the photocatalytic studies, the photocatalyst (100 mg) was dispersed in 100 mL of MB solution (10 mg L^{-1}) with the help of a sonicator for 5 minutes. The resultant solution was loaded into the reactor and then the visible light source is turned on. 5 mL of the reacted MB solution was sampled out periodically and centrifuged in order to remove the catalyst. The absorbance of the supernatant dye solution was measured using a UV-visible spectrometer at 664 nm. The percentage degradation of dye was calculated as per eqn (1).[40]

$$\text{Degradation}\% = [(C_o - C)/C_o] \times 100 \quad (1)$$

where C_o is the initial concentration of the dye solution and C is the concentration at different intervals of time.

2.3 Computational details

The electronic structure of pristine $CaTiO_3$ and V doped $CaTiO_3$ was simulated using an orthorhombic perovskite cell. The DFT calculations carried out using the Quantum ESPRESSO package used pseudopotentials with the Generalized Gradient Approximation (GGA) of Perdew, Burke and Ernzerhof (PBE) functional type.[41,42] The electrons $4s^2$, $3d^24s^2$, $2s^22p^4$, and $3d^34s^2$ of Ca, Ti, O and V, respectively were considered as the valence electrons by the pseudopotential. The plane wave basis representing the wave functions was terminated with an energy cutoff of 50 Ry and charge density cutoff of 400 Ry, respectively. The Brillouin zone was sampled using k point meshes of 8 × 8 × 8 and 16 × 16 × 16 for self-consistent and non-self-consistent field calculations, respectively. The electronic structure was determined along the high symmetry path of Γ–X–S–Y–Γ–Z–U–R–T–Z of the fully relaxed crystal.

3. Results and discussion

3.1 XRD analysis

The XRD diffraction profiles of $CaTiO_3$ and V-doped $CaTiO_3$ can be well matched with the orthorhombic phase of $CaTiO_3$ with JCPDS card number 42-0423 (Fig. 1a). There is no characteristic peak of vanadium oxide in the XRD profiles of V-doped $CaTiO_3$, indicating the successful incorporation of V into the host lattice of $CaTiO_3$. The shift in the 2θ values after V doping is negligible due to the similar radius of V^{4+} and Ti^{4+} ions. If V is doped in the Ca site, then an appreciable shift would have been observed as Ca^{2+} ions are larger in size compared to V^{4+} ions. The average crystallite sizes of the synthesized samples were calculated with the help of the Scherrer equation by using the diffraction angle and full width at half maximum values of the (121) crystal plane.[43] The crystallite sizes were found to be 36.46 nm, 37.45 nm, 44.73 nm, 45.47 nm, 46.23 nm and 47.83 nm for $CaTiO_3$, 0.25 V, 0.5 V, 1.0 V, 1.5 V and 2.0 V, respectively. The increase in the crystallite sizes with increase in doping points towards the increased crystallinity due to favoured directional growth with increase in the concentration of the V dopant.[44,45]

3.2 Morphological and surface area analysis

The morphology of the doped $CaTiO_3$ was studied with the help of field emission scanning electron microscopy (FESEM) and transmission electron microscopy (TEM) analysis. From the FESEM image, we can observe that V doped $CaTiO_3$ has cuboidal morphology (Fig. 2a). This fact is further supported by TEM analysis (Fig. 2b). V doping showed no change in the morphology of $CaTiO_3$. High resolution transmission electron

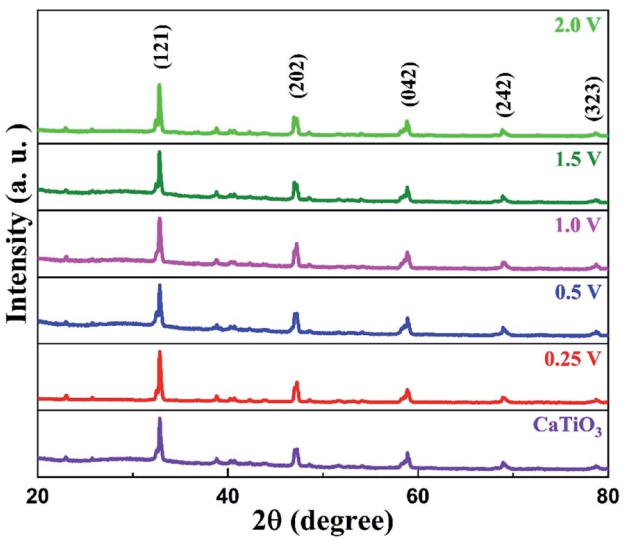

Fig. 1 XRD patterns as a function of the doping concentration of V.

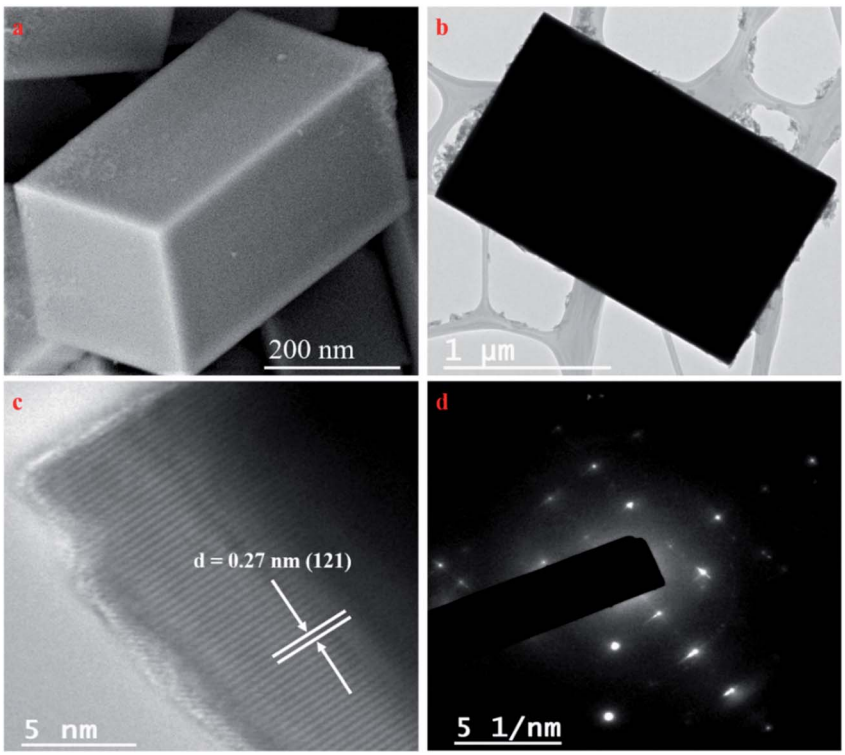

Fig. 2 (a) FESEM image; (b) TEM image; (c) HRTEM image; (d) SAED pattern of 1.0 V.

microscopy (HRTEM) analysis of 1.0 V revealed lattice fringes with 0.27 nm spacing, which could be indexed to the (121) plane of $CaTiO_3$ (Fig. 2c). The selected area electron diffraction (SAED) pattern indicated the single crystalline nature of the material (Fig. 2d). Electron diffraction X-ray (EDX) analysis showed the presence of Ca, Ti, O and V which is in agreement with the obtained X-ray photoelectron spectroscopy (XPS) results (Fig. S1†). Further, elemental mapping of 1.0 V confirms the uniform distribution of atoms in the material (Fig. S2†).

The textural properties of the undoped $CaTiO_3$ and 1.0 V were investigated by BET analysis. The nitrogen adsorption–desorption isotherms indicated a type IV pattern with the hysteresis loops resembling type H3 (P/P_o >0.4), revealing the presence of slit like pores (Fig. 3a and b).[46,47] The BET surface area of 1.0 V was found to be 21.78 $m^2\ g^{-1}$ which is higher in comparison to $CaTiO_3$ (15.88 $m^2\ g^{-1}$), which enables the efficient adsorption and degradation of the pollutants by enhancing the surface-active sites.[48] The pore size distribution was determined using the Barrett–Joyner–Halenda (BJH)

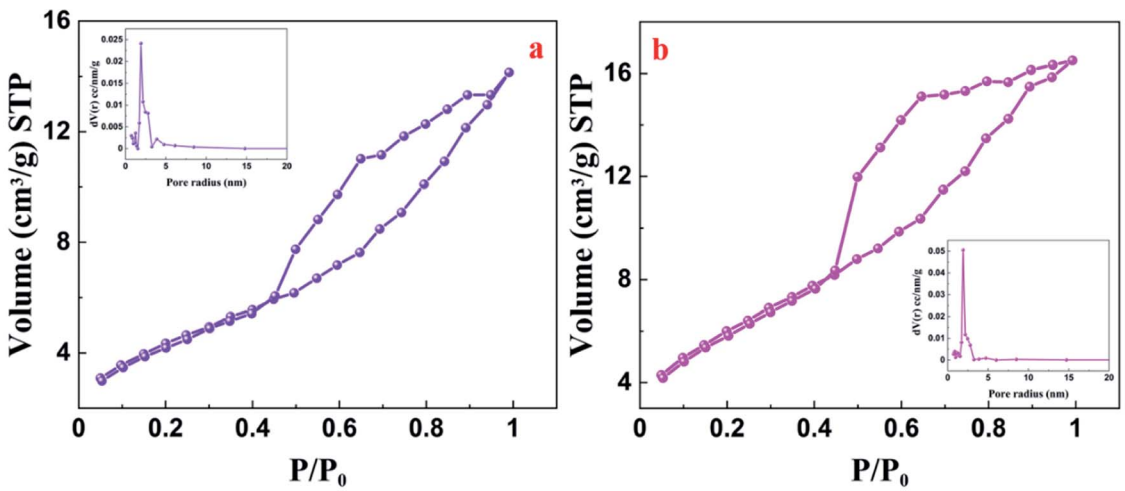

Fig. 3 Nitrogen adsorption–desorption isotherms and BJH pore size distribution (inset) of (a) $CaTiO_3$; (b) 1.0 V.

method.[49] The BJH pore size distributions of the pure $CaTiO_3$ and 1.0 V samples presented a narrow distribution ranging from 3 to 6.6 nm indicating the presence of mesopores (insets of Fig. 3a and b). The pore volume of 1.0 V was found to be 0.0270 $cm^3\ g^{-1}$ which is slightly higher than that of $CaTiO_3$ (0.0240 $cm^3\ g^{-1}$), facilitating effective diffusion of molecules during the photocatalytic reaction.

3.3 XPS analysis

The XPS survey spectrum of $CaTiO_3$ indicated the presence of Ca, Ti and O elements (Fig. S3†). However in the XPS spectrum of 1.0 V we see additional peaks due to V in addition to Ca, Ti and O. The double peaks at the binding energies of 346.7 eV and 350.3 eV could be attributed to Ca $2p_{3/2}$ and Ca $2p_{1/2}$ spin states of Ca^{2+}, respectively in 1.0 V (Fig. 4a).[50] The peaks at the binding energies of 458.8 eV and 464.6 eV could be ascribed to Ti $2p_{3/2}$ and Ti $2p_{1/2}$ states, respectively. These binding energy values confirmed the existence of the +4 oxidation state for Ti in the 1.0 V sample (Fig. 4b).[50,51] Further, it is observed that the shift in the peaks for Ca $2p_{3/2}$ (346.2 eV in $CaTiO_3$) and $2p_{1/2}$ (349.9 eV in $CaTiO_3$) is less compared to Ti $2p_{3/2}$ (458.1 eV in $CaTiO_3$) and Ti $2p_{1/2}$ (464.1 eV in $CaTiO_3$) with V doping indicating that V is doped in the Ti site. The binding energies of 530.2 eV and 531.7 eV could be attributed to O^{2-} in the lattice (O_L) and the hydroxyl groups adsorbed on the surface (O_{OH}), respectively in 1.0 V (Fig. 4c).[35,52] However the same two peaks appear at 529.6 eV and 531.3 eV, respectively in $CaTiO_3$. The double peaks at the binding energies of 515.9 eV and 523.3 eV could be ascribed to V $2p_{3/2}$ and V $2p_{1/2}$ states, respectively, indicating the oxidation state of V as +4 (Fig. 4d) and successful incorporation of V in $CaTiO_3$.[35,53–55] The maintenance of charge neutrality in the crystal thus avoids the formation of defect states and hence prevents recombination of charge carriers and enhances the carrier lifetime.

3.4 Electronic structure analysis

$CaTiO_3$, a perovskite material can occur in either cubic structure or orthorhombic structure. Since the experimental results indicated that the material was in the orthorhombic phase, the electronic structure and density of states (DOS) of $CaTiO_3$ were simulated using the pristine orthorhombic structure containing 20 atoms (Fig. 5a). The estimated lattice parameters of the fully relaxed parent $CaTiO_3$ were found to be $a = 5.399$ Å, $b = 5.499$ Å and $c = 7.683$ Å, respectively. Fig. 5b reveals a direct band gap of

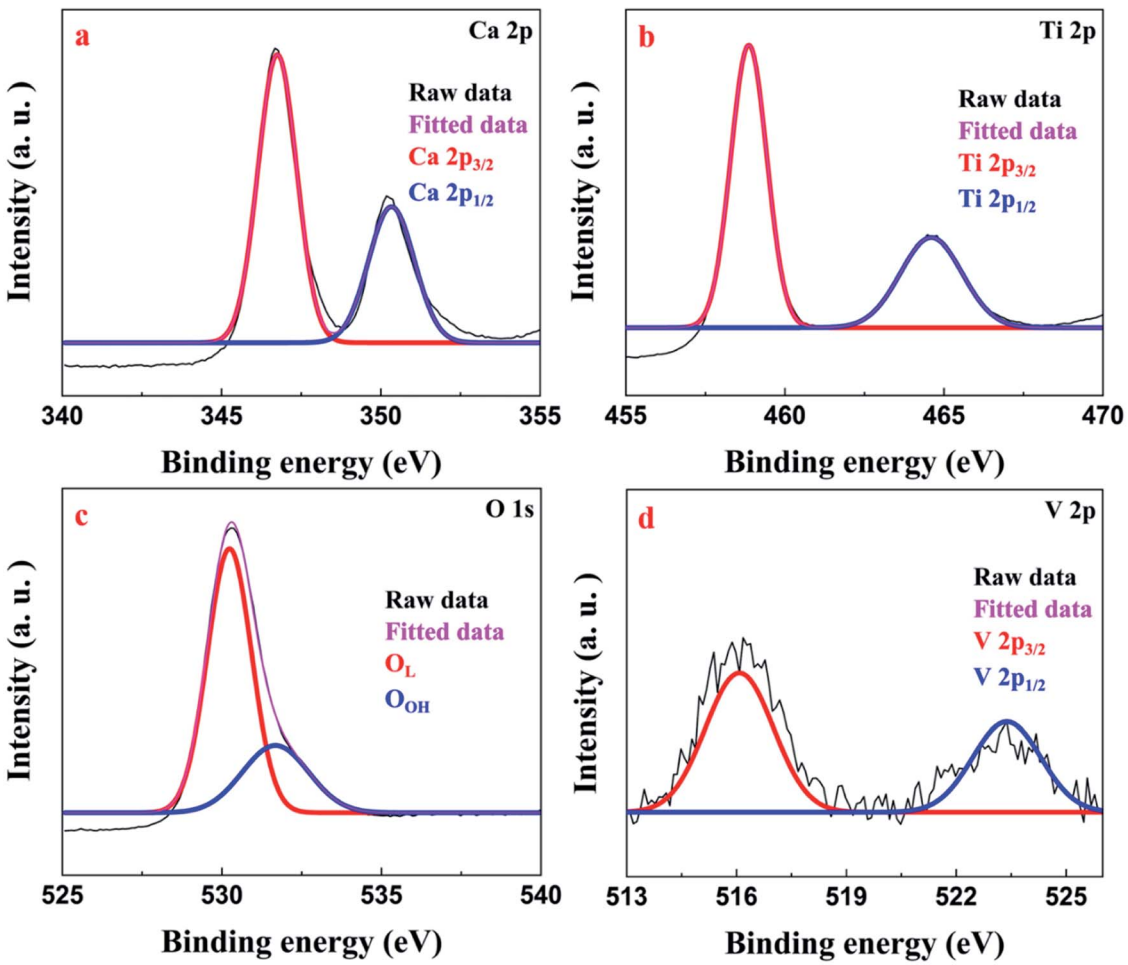

Fig. 4 High resolution XPS spectrum of 1.0 V (a) Ca 2p; (b) Ti 2p; (c) O 1s; (d) V 2p.

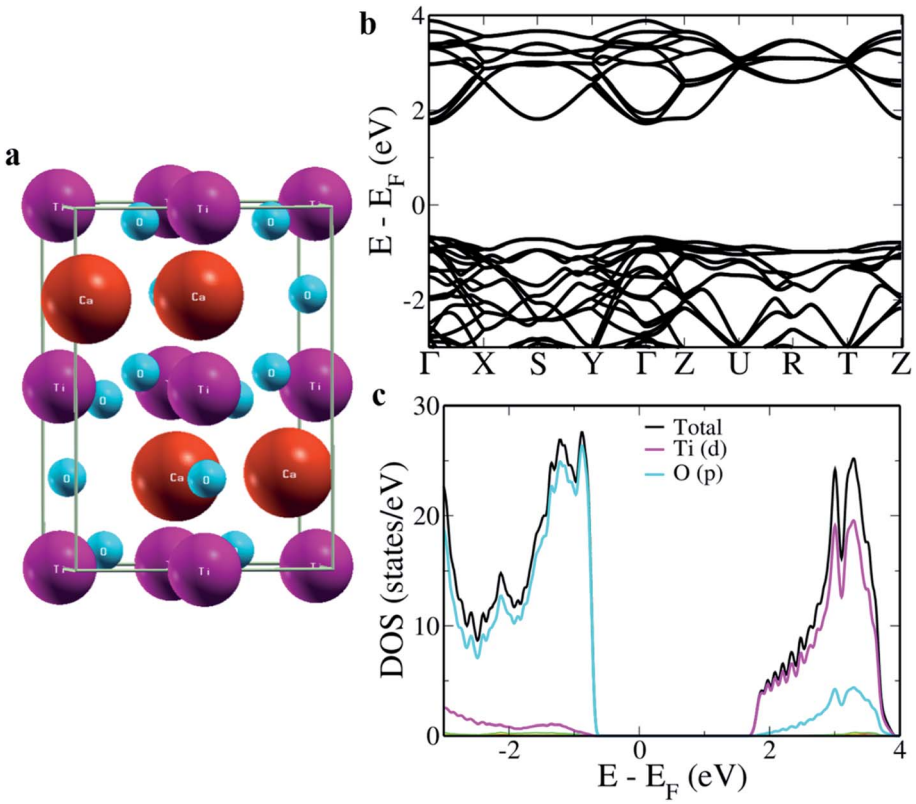

Fig. 5 (a) Crystal structure; (b) electronic structure; (c) pDOS of $CaTiO_3$.

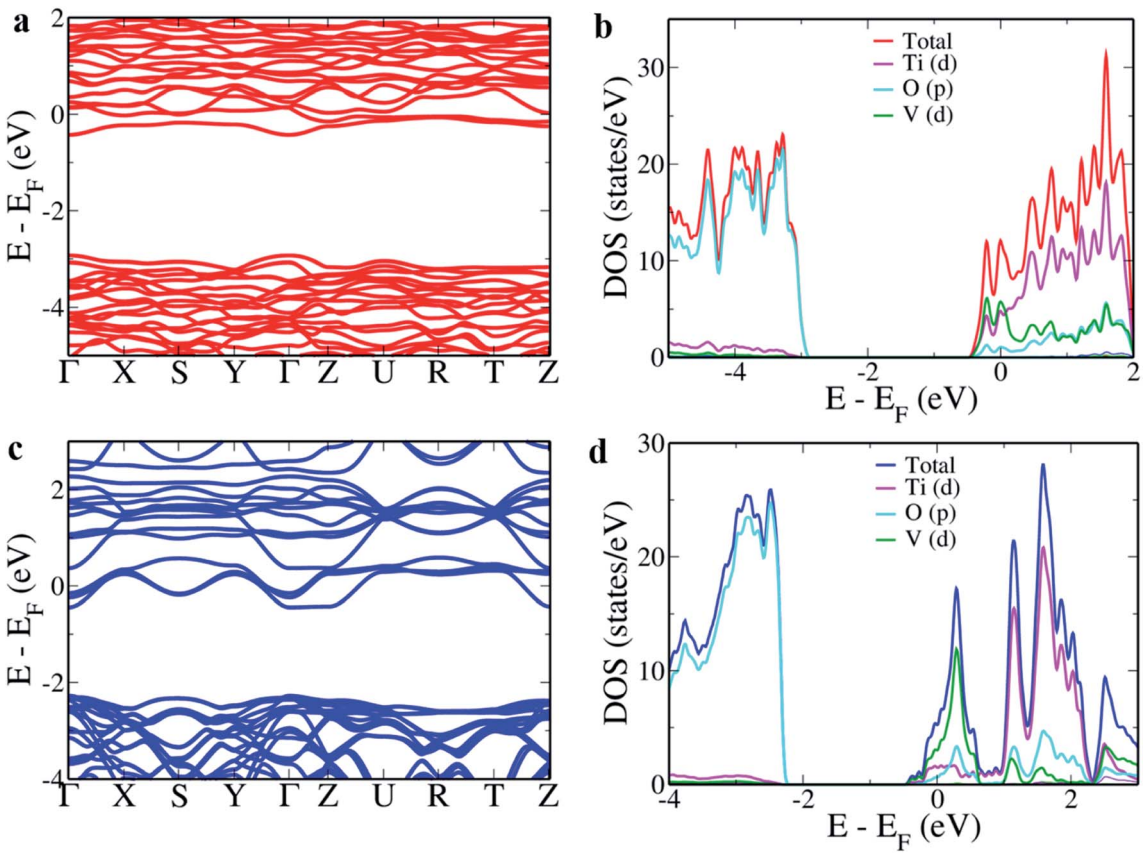

Fig. 6 Electronic structure and pDOS of V doped $CaTiO_3$ (a and b) V in the Ca site; (c and d) V in the Ti site.

2.397 eV at the Γ point. Such an underestimation of the band gap is typical of DFT calculations due to the presence of discontinuities in the derivative of energy with respect to the number of electrons.[56,57] The contribution of the various atoms to the electronic structure was studied by projecting the atomic orbitals onto the DOS. Fig. 5c indicates that the O 'p' orbitals mainly contribute towards the valence band (VB) while the 'd' orbitals of Ti form the conduction band (CB) similar to the case of $SrTiO_3$ and $BaTiO_3$.[36,37]

The site occupied by the dopant largely effects its electronic structure and properties.[25,58] Since there are two possible cationic doping sites for V, both were simulated. Doping V in Ca sites led to a decrease in '*a*' and '*c*' lattice parameters to 5.371 Å and 7.671 Å, respectively while the '*b*' parameter increased to 5.590 Å. It is observed that when V goes into the Ca site the band gap decreases to 2.501 eV at the Γ point (Fig. 6a). This is due to the 'd' states of V which pull the Ti 'd' states lower (Fig. 6b). Substitution of V in the Ti site decreased the cell volume by decreasing the lattice parameters to $a = 5.383$ Å, $b = 5.475$ Å and $c = 7.652$ Å, respectively. V in the Ti site leads to the formation of an energy band just beneath the CB decreasing the band gap at the Γ point to 1.832 eV. This band is formed due to the hybridization of 'd' states of V with 'p' states of O with a bandwidth of 1.029 eV. The continuous nature of the additional band with the conduction states leads to easy migration of charge carriers, effectively separating the electrons and holes avoiding the recombination.[25] The results also indicate that directing V into the Ti site would be more beneficial for photocatalytic application due to the higher amount of decrease in the band gap.

3.5 Optical absorbance analysis

As shown in Fig. 7a, the absorption edge of V-doped $CaTiO_3$ was red shifted as compared to pristine $CaTiO_3$. This could be attributed to the insertion of the t_{2g} level of the V 3d orbital within the band gap as discussed in the previous section. The absorption data were derived using the Kubelka–Munk equation (eqn (2)).[58,59]

$$A/S = \frac{(1-R)^2}{2R} \quad (2)$$

where R is the reflectance, and A and S are the absorption and scattering coefficients. The band gap was determined from the plot of A/S *versus* energy (Fig. 7b). The band gap energies of $CaTiO_3$, 0.25 V, 0.5 V, 1.0 V, 1.5 V and 2.0 V were found to be 3.24 eV, 2.2 eV, 2.12 eV, 2.02 eV, 1.92 eV and 1.83 eV, respectively.

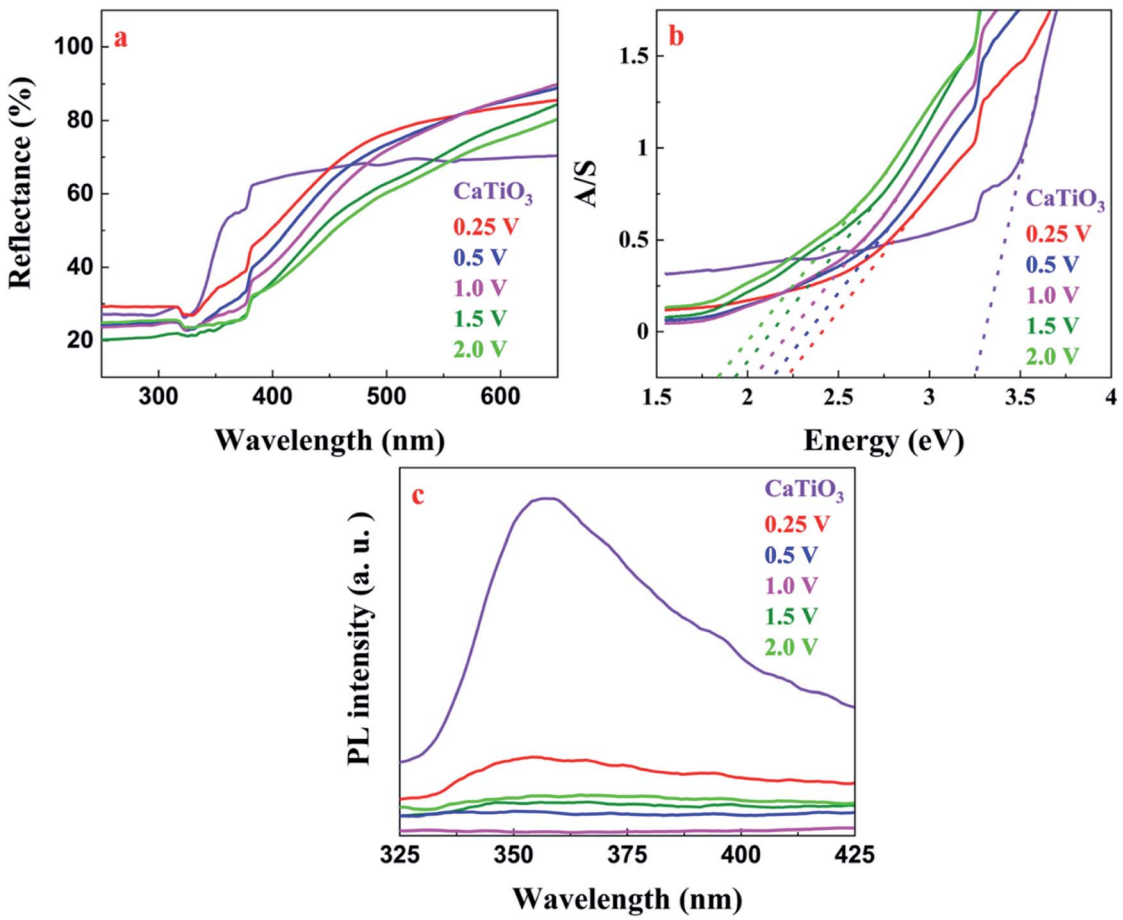

Fig. 7 (a) UV-visible DR spectra; (b) electronic absorption spectra; (c) PL spectra of $CaTiO_3$ and V-doped $CaTiO_3$ samples.

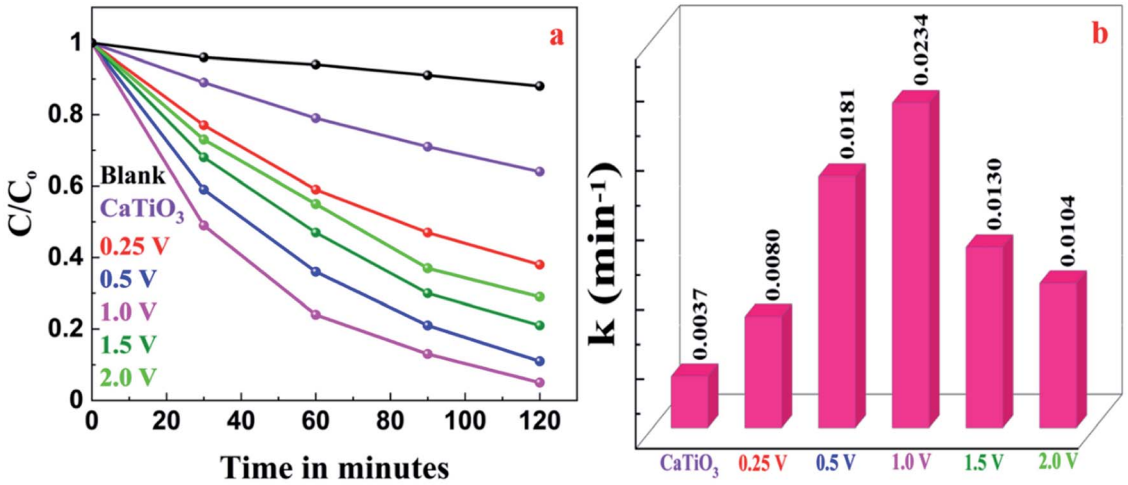

Fig. 8 (a) The photocatalytic degradation curves of MB; (b) the rate constants of the photocatalytic degradation of MB by the synthesized $CaTiO_3$ and V doped $CaTiO_3$.

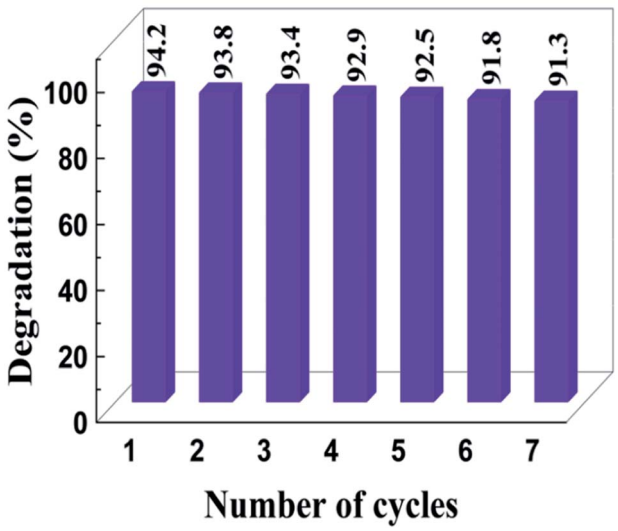

Fig. 9 Cycling stability of the synthesized 1.0 V.

PL analysis was carried out in order to get more insight into defect chemistry and charge recombination behaviour of the synthesized materials.[60] As shown in Fig. 7c, the V doped $CaTiO_3$ sample exhibited inferior fluorescence intensity in comparison to pristine $CaTiO_3$ which could be attributed to the incorporation of V in the isovalent state, thus suppressing the formation of the recombination centres. Among the different samples, 1.0 V showed the least PL intensity and as a result, it is expected to show the highest photocatalytic activity.

3.6 Photocatalytic activity

The photocatalytic activity of the synthesized catalysts was evaluated for the degradation of MB dye solution under visible light. Fig. 8a shows the photocatalytic degradation of MB as a function of irradiation time in the presence of $CaTiO_3$ and V-doped $CaTiO_3$ samples. The photocatalytic activity of V-doped $CaTiO_3$ samples was found to be higher than that of $CaTiO_3$ which could be attributed to the introduction of additional energy levels just beneath the CB effectively decreasing the band gap and reduction in the recombination of photoinduced charges due to efficient charge separation. Among the various V-doped samples, 1.0 V exhibited the highest photocatalytic activity, beyond which the photocatalytic activity decreases. This reduction in the photocatalytic activity can be attributed to the formation of recombination centres as confirmed by PL analysis. In addition to this, the 1.0 V sample exhibited higher surface area which enables the efficient adsorption and degradation of the pollutants during the photocatalytic reaction. It is observed that the adsorption capacity is almost three times higher for 1.0 V compared to $CaTiO_3$ (Fig. S4†). Comparison of the photocatalytic activity of 1.0 V with the previously reported ones show that our material is highly efficient (Table S1†).[24,25,30,32,35,50,51,61–65]

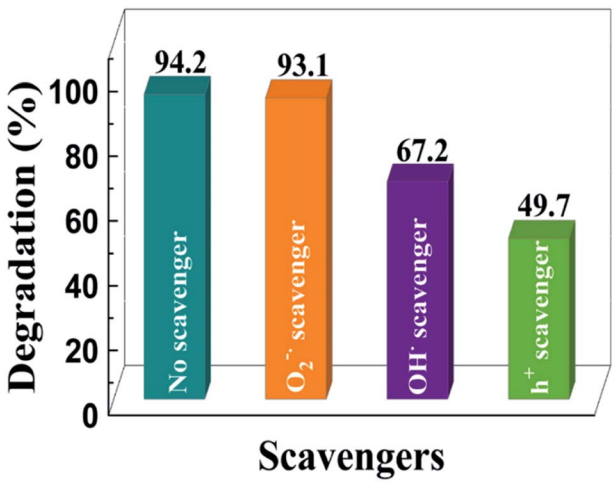

Fig. 10 Effect of radical scavengers on the photocatalytic degradation of MB by 1.0 V.

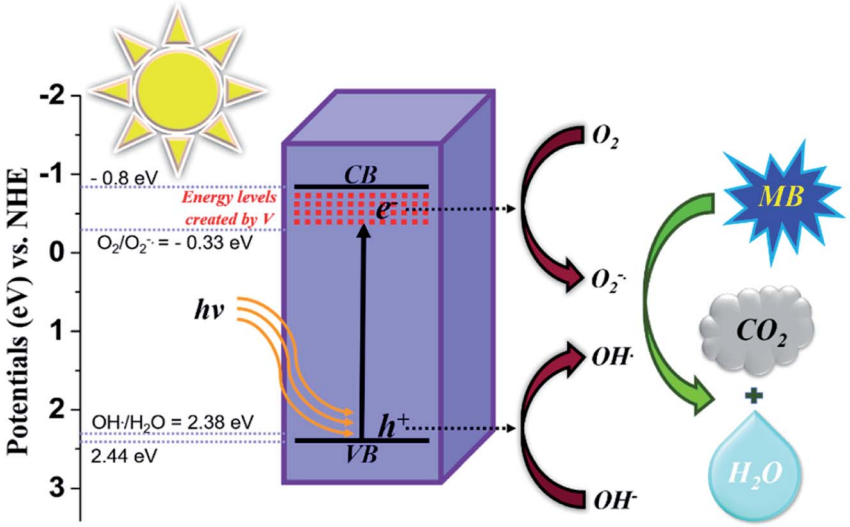

Fig. 11 Proposed mechanism for the photocatalytic degradation of MB under visible light irradiation.

The degradation kinetics of MB by $CaTiO_3$ and V-doped $CaTiO_3$ is well fitted with the pseudo first-order rate equation given by (3).[66]

$$-\ln(C/C_o) = kt \quad (3)$$

where C_o is the initial concentration of the dye, C is the concentration of the dye at irradiation time 't' and 'k' is the first order rate constant. 'k' is calculated from the slope of the linear fit of $-\ln(C/C_o)$ *versus* 't'. The rate constant of 1.0 V was found to be higher than that of all the other samples indicating the higher efficiency of the material (Fig. 8b). Further, 1.0 V exhibited high stability towards the photocatalytic degradation reactions as 1.0 V just showed a slight decline in the photocatalytic activity even after seven consecutive cycles (Fig. 9).

Trapping experiments were carried out in order to assess the active species involved in the photocatalytic degradation by following the same procedure as that of photocatalytic activity evaluation in the presence of different radical scavenging agents such as benzoquinone (1 mM) as a superoxide anion radical ($O_2^{-\bullet}$) scavenger, potassium iodide (10 mM) as a hole (h^+) scavenger and isopropyl alcohol (10 mM) as a hydroxyl radical ($OH^\bullet$) scavenger.[26] From Fig. 10 it can be seen that superoxide anion radicals are not the major active species as the corresponding scavenger benzoquinone did not deteriorate the photocatalytic activity much. This is also confirmed by the band edge positions as a decrease in the band gap with V doping brings the potential of the CB lower than the potential for the generation of superoxide anion radicals. Further, the addition of potassium iodide (hole scavenger) and isopropyl alcohol ($OH^\bullet$ scavenger) reduced the photocatalytic activity significantly. As a result, holes followed by hydroxyl radicals are considered to be the active species for the effective degradation of the dye.

The mechanism of photocatalytic degradation of MB can be stated as follows: when V doped $CaTiO_3$ is irradiated with an energy equal to or greater than its band gap, electrons from the VB get excited to the energy levels created by V just beneath the CB edge generating corresponding number of holes in the VB. These electrons react with oxygen to produce superoxide radicals ($O_2^{-\bullet}$). The holes in the VB either directly react with MB or react with surface hydroxyl groups to produce hydroxyl radicals ($OH^\bullet$).[25] The formed radicals are said to be active species for the effective degradation of MB to carbon dioxide and water (Fig. 11).

The thermodynamic parameters such as, activation energy (E_a), free energy of activation ($\Delta G^\#$), enthalpy of activation ($\Delta H^\#$) and entropy of activation ($\Delta S^\#$) were computed by employing activation complex theory and the Eyring equation.[35,51] From the values tabulated we observe that higher energy of activation is required for the photodegradation of MB without the catalyst, whereas a relatively lower energy of activation is needed in the presence of $CaTiO_3$ and V-doped $CaTiO_3$ catalysts (Table 1). This confirms that the catalyst alters the path of the reaction by lowering the activation energy barrier. The 1.0 V sample exhibited the lowest activation energy as compared to other samples. The endothermic and non-spontaneous nature of the reaction was indicated by the positive enthalpy and free energy change.

Table 1 Thermodynamic parameters of $CaTiO_3$ and V doped $CaTiO_3$ samples

Sample	E_a (kJ mol^{-1})	$\Delta H^\#$ (kJ mol^{-1})	$\Delta S^\#$ (kJ mol^{-1})	$\Delta G^\#$ (kJ mol^{-1})
Without catalyst	17.7	15.2	−0.25	91.2
$CaTiO_3$	13.9	11.5	−0.25	87.4
0.25 V	12.0	9.5	−0.25	85.5
0.5 V	10.0	7.5	−0.25	83.5
1.0 V	9.4	6.9	−0.25	82.8
1.5 V	10.8	8.3	−0.25	84.3
2.0 V	11.4	8.9	−0.25	84.9

4. Conclusions

V doped $CaTiO_3$ was successfully synthesized by a simple one pot solvothermal approach by avoiding high temperature calcination. The present synthetic strategy involves incorporation of V^{4+} ions into the Ti sites of $CaTiO_3$ with high surface area, as confirmed by XRD, XPS and BET results. First principles DFT calculations showed that the band gap of the doped samples decreased due to the formation of additional energy levels just beneath the conduction band. The PL results indicated the efficient charge separation due to the isovalent doping thereby boosting the photocatalytic efficiency. The superior photocatalytic activity and high stability of V doped $CaTiO_3$ (1.0 V) for MB degradation reveal that the material can be a promising catalyst for photocatalytic water treatment.

Conflicts of interest

There are no conflicts of interest to declare.

References

1 Q. Lei, S. Yang, D. Ding, J. Tan, J. Liu and R. Chen, Local-interaction-field-coupled semiconductor photocatalysis: recent progress and future challenges, *J. Mater. Chem. A*, 2021, **9**, 2491–2525.

2 D. K. Bhat and U. S. Shenoy, SnTe thermoelectrics: dual step approach for enhanced performance, *J. Alloys Compd.*, 2020, **834**, 155181.

3 X. Li, H. Zhao, J. Liang, Y. Luo, G. Chen, X. Shi, S. Lu, S. Gao, J. Hu, Q. Liu and X. Sun, A-site perovskite oxides: an emerging functional material for electrocatalysis and photocatalysis, *J. Mater. Chem. A*, 2021, **9**, 6650–6670.

4 U. S. Shenoy and D. K. Bhat, Electronic structure engineering of $SrTiO_3$ *via* rhodium doping: a DFT study, *J. Phys. Chem. Solids*, 2021, **148**, 109708.

5 R. Shen, D. Ren, Y. Ding, Y. Guan, Y. H. Ng, P. Zhang and X. Li, Nanostructured CdS for efficient photocatalytic H_2 evolution: a review, *Sci. China Mater.*, 2020, **63**, 2153–2188.

6 D. Ren, R. Shen, Z. Jiang, X. Lu and X. Li, Highly efficient visible-light photocatalytic H_2 evolution over 2D–2D CdS/Cu_7S_4 layered heterojunctions, *Chin. J. Catal.*, 2020, **41**, 31–40.

7 R. Zhang, C. Wang, H. Chen, H. Zhao, J. Liu, Y. Li and B. Su, Cadmium sulfide inverse opal for photocatalytic hydrogen roduction, *Acta Phys.-Chim. Sin.*, 2020, **36**, 1803014.

8 D. K. Bhat and U. S. Shenoy, Resonance levels in GeTe thermoelectrics: zinc as a new multifaceted dopant, *New J. Chem.*, 2020, **44**, 17664–17670.

9 Z. Wei, M. Xu, J. Liu, W. Guo, Z. Jiang and W. Shangguan, Simultaneous visible-light-induced hydrogen production enhancement and antibiotic wastewater degradation using MoS_2@$Zn_xCd_{1-x}S$: solid-solution-assisted photocatalysis, *Chin. J. Catal.*, 2020, **41**, 103–113.

10 Z. Liang, R. Shen, Y. H. Ng, P. Zhang, Q. Xiang and X. Li, A review on 2D MoS_2 cocatalysts in photocatalytic H_2 production, *J. Mater. Sci. Technol.*, 2020, **56**, 89–121.

11 U. S. Shenoy and D. K. Bhat, Bi and Zn co-doped SnTe thermoelectrics: interplay of resonance levels and heavy hole band dominance leading to enhanced performance and a record high room temperature ZT, *J. Mater. Chem. C*, 2020, **8**, 2036–2042.

12 D. K. Bhat and U. S. Shenoy, Mg/Ca doping ameliorates the thermoelectric properties of GeTe: influence of electronic structure engineering, *J. Alloys Compd.*, 2020, **843**, 155989.

13 R. Gusain, K. Gupta, P. Joshi and O. P. Khatri, Adsorptive removal and photocatalytic degradation of organic pollutants using metal oxides and their composites: a comprehensive review, *Adv. Colloid Interface Sci.*, 2019, **272**, 102009.

14 M. M. J. Sadiq, U. S. Shenoy and D. K. Bhat, Enhanced photocatalytic performance of *N*-doped RGO-$FeWO_4$/Fe_3O_4 ternary nanocomposite in environmental applications, *Mater. Today Chem.*, 2017, **4**, 133–141.

15 P. Raizada, S. Sharma, A. Kumar, P. Singh, A. A. P. Khan and A. M. Asiri, Performance improvement strategies of $CuWO_4$ photocatalyst for hydrogen generation and pollutant degradation, *J. Environ. Chem. Eng.*, 2020, **8**, 104230.

16 F. Dai, Y. Wang, R. Zhao, X. Zhou, J. Han and L. Wang, $ZnIn_2S_4$ modified $CaTiO_3$ nanocubes with enhanced photocatalytic hydrogen performance, *Int. J. Hydrogen Energy*, 2020, **45**, 28783–28791.

17 A. Kumar, V. Navakoteswara Rao, A. Kumar, M. Venkatakrishnan Shankar and V. Krishnan, Interplay between mesocrystals of $CaTiO_3$ and edge sulfur atom enriched MoS_2 on reduced graphene oxide nanosheets: enhanced photocatalytic performance under sunlight irradiation, *ChemPhotoChem*, 2020, **4**, 427–444.

18 Y. Yan, H. Yang, Z. Yi, R. Li and T. Xian, Design of ternary $CaTiO_3$/g-C_3N_4/AgBr Z-scheme heterostructured photocatalysts and their application for dye photodegradation, *Solid State Sci.*, 2020, **100**, 106102.

19 M. M. J. Sadiq, U. S. Shenoy and D. K. Bhat, Synthesis of $BaWO_4$/NRGO–gC_3N_4 nanocomposites with excellent multifunctional catalytic performance *via* microwave approach, *Front. Mater. Sci.*, 2018, **12**, 247–263.

20 S. Wageh, A. A. Al-Ghamdi, R. Jafer, X. Li and P. Zhang, A new heterojunction in photocatalysis: S-scheme heterojunction, *Chin. J. Catal.*, 2021, **42**, 667–669.

21 D. Cao, H. An, X. Yan, Y. Zhao, G. Yang and H. Mei, Fabrication of Z-scheme heterojunction of SiC/Pt/CdS nanorod for efficient photocatalytic H_2 evolution, *Acta Phys.-Chim. Sin.*, 2020, **36**, 1901051–1901059.

22 E. Jiang, L. Yang, N. Song, X. Zhang, C. Liu and H. Dong, Multi-shelled hollow cube $CaTiO_3$ decorated with $Bi_{12}O_{17}Cl_2$ towards enhancing photocatalytic performance under the visible light, *J. Colloid Interface Sci.*, 2020, **576**, 21–33.

23 M. Shi, B. Rhimi, K. Zhang, J. Xu, D. W. Bahnemann and C. Wang, Visible light-driven novel $Bi_2Ti_2O_7$/$CaTiO_3$ composite photocatalyst with enhanced photocatalytic activity towards NO removal, *Chemosphere*, 2021, **275**, 130083.

24 M. Chen, Q. Xiong, Z. Liu, K. Qiu and X. Xiao, Synthesis and photocatalytic activity of Na^+ Co-doped $CaTiO_3$: Eu^{3+} photocatalysts for methylene blue degradation, *Ceram. Int.*, 2020, **46**, 12111–12119.

25 U. S. Shenoy, H. Bantawal and D. K. Bhat, Band engineering of $SrTiO_3$: effect of synthetic technique and site occupancy of doped rhodium, *J. Phys. Chem. C*, 2018, **122**, 27567–27574.

26 H. Bantawal, M. Sethi, U. S. Shenoy and D. K. Bhat, Porous graphene wrapped $SrTiO_3$ nanocomposite: Sr–C bond as an effective coadjutant for high performance photocatalytic degradation of methylene blue, *ACS Appl. Nano Mater.*, 2019, **2**, 6629–6636.

27 H. Zhang, G. Chen, X. He and J. Xu, Electronic structure and photocatalytic properties of Ag–La codoped $CaTiO_3$, *J. Alloys Compd.*, 2012, **516**, 91–95.

28 R. Wang, S. Ni, G. Liu and X. Xu, Hollow $CaTiO_3$ cubes modified by La/Cr Co-doping for efficient photocatalytic hydrogen production, *Appl. Catal., B*, 2018, **225**, 139–147.

29 H. Zhang, G. Chen, Y. Li and Y. Teng, Electronic structure and photocatalytic properties of copper-doped $CaTiO_3$, *Int. J. Hydrogen Energy*, 2010, **35**, 2713–2716.

30 L. M. Lozano-Sánchez, S. Obregón, L. A. Díaz-Torres, S. W. Lee and V. Rodríguez-González, Visible and near-infrared light-driven photocatalytic activity of erbium-doped $CaTiO_3$ system, *J. Mol. Catal.*, 2015, **410**, 19–25.

31 B. G. Park, Photoluminescence of Eu^{3+}-doped $CaTiO_3$ perovskites and their photocatalytic properties with a metal ion loading, *Chem. Phys. Lett.*, 2019, **722**, 44–49.

32 H. Yang, C. Han and X. Xue, Photocatalytic activity of Fe-doped $CaTiO_3$ under UV–visible light, *J. Environ. Sci.*, 2014, **26**, 1489–1495.

33 J. Wang, F. Han, Y. Rao, T. Hu, Y. Huang, J. J. Cao and S. C. Lee, Visible-light-driven nitrogen-doped carbon quantum dots/$CaTiO_3$ composite catalyst with enhanced NO adsorption for NO removal, *Ind. Eng. Chem. Res.*, 2018, **57**, 10226–10233.

34 X. J. Huang, Y. A. N. Xin, H. Y. Wu, F. A. N. G. Ying, Y. H. Min, W. S. Li, S. Y. Wang and Z. J. Wu, Preparation of Zr-doped $CaTiO_3$ with enhanced charge separation efficiency and photocatalytic activity, *Trans. Nonferrous Met. Soc.*, 2016, **26**, 464–471.

35 H. Bantawal, U. S. Shenoy and D. K. Bhat, Vanadium-doped $SrTiO_3$ nanocubes: insight into role of vanadium in improving the photocatalytic activity, *Appl. Surf. Sci.*, 2020, **513**, 145858.

36 U. S. Shenoy and D. K. Bhat, Enhanced thermoelectric properties of vanadium doped $SrTiO_3$: a resonant dopant approach, *J. Alloys Compd.*, 2020, **832**, 154958.

37 U. S. Shenoy and D. K. Bhat, Vanadium doped $BaTiO_3$ as high performance thermoelectric material: role of electronic structure engineering, *Mater. Today Chem.*, 2020, **18**, 100384.

38 C. E. Choong, K. T. Wong, H. Kim, S. B. Jang, S. Y. Yoon, I. W. Nah, W. Kim, S. H. Kim, B. H. Jeon, Y. Yoon and M. Jang, Unexpected discovery of superoxide radical generation by oxygen vacancies containing biomass derived granular activated carbon, *Water Res.*, 2020, **190**, 116757.

39 H. Bantawal, U. S. Shenoy and D. K. Bhat, Tuning the photocatalytic activity of $SrTiO_3$ by varying the Sr/Ti Ratio: unusual effect of viscosity of the synthesis medium, *J. Phys. Chem. C*, 2018, **122**, 20027–20033.

40 M. J. S. Mohamed, S. Shenoy and D. K. Bhat, Novel NRGO–$CoWO_4$–Fe_2O_3 nanocomposite as an efficient catalyst for dye degradation and reduction of 4-nitrophenol, *Mater. Chem. Phys.*, 2018, **208**, 112–122.

41 P. Giannozzi, S. Baroni, N. Bonini, M. Calandra, R. Car, C. Cavazzoni, D. Ceresoli, G. L. Chiarotti, M. Cococcioni, I. Dabo, A. L. Corso, S. de Gironcoli, S. Fabris, G. Fratesi, R. Gebauer, U. Gerstmann, C. Gougoussis, A. Kokalj, M. Lazzeri, L. Martin-Samos, N. Marzari, F. Mauri, R. Mazzarello, S. Paolini, A. Pasquarello, L. Paulatto, C. Sbraccia, S. Scandolo, G. Sclauzero, A. P. Seitsonen, A. Smogunov, P. Umari and R. M. Wentzcovitch, Quantum ESPRESSO: a modular and open-source software project for quantum simulations of materials, *J. Phys.: Condens. Matter*, 2009, **21**, 395502.

42 J. P. Perdew, K. Burke and M. Ernzerhof, Generalized gradient approximation made simple, *Phys. Rev. Lett.*, 1996, **77**, 3865.

43 M. Sethi and D. K. Bhat, Facile solvothermal synthesis and high supercapacitor performance of $NiCo_2O_4$ nanorods, *J. Alloys Compd.*, 2019, **781**, 1013–1020.

44 B. Liu, X. Wang, G. Cai, L. Wen, Y. Song and X. Zhao, Low temperature fabrication of V-doped TiO_2 nanoparticles, structure and photocatalytic studies, *J. Hazard. Mater.*, 2009, **169**, 1112–1118.

45 J. C. S. Wu and C. H. Chen, A visible-light response vanadium-doped titania nanocatalyst by sol–gel method, *J. Photochem. Photobiol., A*, 2004, **163**, 509–515.

46 M. Sethi, U. S. Shenoy and D. K. Bhat, A porous graphene–$NiFe_2O_4$ nanocomposite with high electrochemical performance and high cycling stability for energy storage applications, *Nanoscale Adv.*, 2020, **2**, 4229–4241.

47 D. Ren, Z. Liang, Y. H. Ng, P. Zhang, Q. Xiang and X. Li, Strongly coupled 2D–2D nanojunctions between P-doped Ni_2S (Ni_2SP) cocatalysts and CdS nanosheets for efficient photocatalytic H_2 evolution, *Chem. Eng. J.*, 2020, **390**, 124496.

48 M. E. Malefane, Co_3O_4/$Bi_4O_5I_2$/Bi_5O_7I C-scheme heterojunction for degradation of organic pollutants by light-emitting diode irradiation, *ACS Omega*, 2020, **5**, 26829–26844.

49 M. Sethi, U. S. Shenoy and D. K. Bhat, Simple solvothermal synthesis of porous graphene-NiO nanocomposites with high cyclic stability for supercapacitor application, *J. Alloys Compd.*, 2021, **854**, 157190.

50 E. Jiang, N. Song, G. Che, C. Liu, H. Dong and L. Yang, Construction of a Z-scheme MoS_2/$CaTiO_3$ heterostructure by the morphology-controlled strategy towards enhancing photocatalytic activity, *Chem. Eng. J.*, 2020, **399**, 125721.

51 D. K. Bhat, H. Bantawal and U. S. Shenoy, Rhodium doping augments photocatalytic activity of barium titanate: effect of

electronic structure engineering, *Nanoscale Adv.*, 2020, **2**, 5688–5698.

52 J. Cai, A. Cao, J. Huang, W. Jin, J. Zhang, Z. Jiang and X. Li, Understanding oxygen vacancies in disorder-engineered surface and subsurface of $CaTiO_3$ nanosheets on photocatalytic hydrogen evolution, *Appl. Catal., B*, 2020, **267**, 118378.

53 I. Top, R. Binions, M. E. Warwick, C. W. Dunnill, M. Holdynski and I. Abrahams, VO_2/TiO_2 bilayer films for energy efficient windows with multifunctional properties, *J. Mater. Chem. C*, 2018, **6**, 4485–4493.

54 S. P. Vattikuti, A. K. R. Police, J. Shim and C. Byon, *In situ* fabrication of the Bi_2O_3–V_2O_5 hybrid embedded with graphitic carbon nitride nanosheets: oxygen vacancies mediated enhanced visible-light–driven photocatalytic degradation of organic pollutants and hydrogen evolution, *Appl. Surf. Sci.*, 2018, **447**, 740–756.

55 Y. Li, D. Gu, S. Xu, X. Zhou, K. Yuan and Y. Jiang, A monoclinic $V_{1-xy}Ti_xRu_yO_2$ thin film with enhanced thermal-sensitive performance, *Nanoscale Res. Lett.*, 2020, **15**, 1–10.

56 D. K. Bhat and U. S. Shenoy, Zn: a versatile resonant dopant for SnTe thermoelectrics, *Mater. Today Phys.*, 2019, **11**, 100158.

57 U. S. Shenoy and D. K. Bhat, Electronic structure modulation of $Pb_{0.6}Sn_{0.4}Te$ *via* zinc doping and its effect on the thermoelectric properties, *J. Alloys Compd.*, 2021, **872**, 159681.

58 U. S. Shenoy and D. K. Bhat, Enhanced bulk thermoelectric performance of $Pb_{0.6}Sn_{0.4}Te$: effect of magnesium doping, *J. Phys. Chem. C*, 2017, **121**, 20696–20703.

59 L. Zhiming, L. Guoliang and H. Xinlin, Influence of surface defects and palladium deposition on the activity of CdS nanocrystals for photocatalytic hydrogen production, *Acta Phys.-Chim. Sin.*, 2019, **35**, 215–222.

60 R. Shen, Y. Ding, S. Li, P. Zhang, Q. Xiang, Y. H. Ng and X. Li, Constructing low-cost Ni_3C/twin-crystal $Zn_{0.5}Cd_{0.5}S$ heterojunction/homojunction nanohybrids for efficient photocatalytic H_2 evolution, *Chin. J. Catal.*, 2021, **42**, 25–36.

61 C. Han, J. Liu, W. Yang, Q. Wu, H. Yang and X. Xue, Enhancement of photocatalytic activity of $CaTiO_3$ through HNO_3 acidification, *J. Photochem. Photobiol.*, 2016, **322**, 1–9.

62 A. Kumar, S. Kumar, A. Bahuguna, A. Kumar, V. Sharma and V. Krishnan, Recyclable, bifunctional composites of perovskite type N-$CaTiO_3$ and reduced graphene oxide as an efficient adsorptive photocatalyst for environmental remediation, *Mater. Chem. Front.*, 2017, **1**, 2391–2404.

63 Y. Yan, H. Yang, X. Zhao, R. Li and X. Wang, Enhanced photocatalytic activity of surface disorder-engineered $CaTiO_3$, *Mater. Res. Bull.*, 2018, **105**, 286–290.

64 Y. Yan, H. Yang, Z. Yi, R. Li and X. Wang, Enhanced photocatalytic performance and mechanism of Au@$CaTiO_3$ composites with Au nanoparticles assembled on $CaTiO_3$ nanocuboids, *Micromachines*, 2019, **10**, 254.

65 X. Chen, X. He, X. Yang, Z. Wu and Y. Li, Construction of novel 2D/1D g–C_3N_4/$CaTiO_3$ heterojunction with face-to-face contact for boosting photodegradation of triphenylmethane dyes under simulated sunlight, *J. Taiwan Inst. Chem. Eng.*, 2020, **107**, 98–109.

66 M. M. J. Sadiq, U. S. Shenoy and D. K. Bhat, $NiWO_4$–ZnO–NRGO ternary nanocomposite as an efficient photocatalyst for degradation of methylene blue and reduction of 4-nitro phenol, *J. Phys. Chem. Solids*, 2017, **109**, 124–133.